Characterization of high-intensity laser propagation in the relativistic transparent regime through measurements of energetic proton beams

L. Willingale[1], S. R. Nagel[1], A. G. R. Thomas[1], C. Bellei[1], R. J. Clarke[2], A. E. Dangor[1], R. Heathcote[2], M. C. Kaluza[1†], C. Kamperidis[1], S. Kneip[1], K. Krushelnick[1*], N. Lopes[3], S. P. D. Mangles[1], W. Nazarov[4], P. M. Nilson[1‡], and Z. Najmudin[1]

[1] *Blackett Laboratory, Imperial College, London SW7 2AZ, United Kingdom*

[2] *Central Laser Facility, Rutherford-Appleton Laboratory, Chilton, Oxon, OX11 0QX, United Kingdom*

[3] *GoLP, Instituto Superior Tecnico, Lisbon, Portugal and*

[4] *University of St. Andrews, Fife, KY16 9ST, United Kingdom*

(Dated: October 10, 2008)

Experiments were performed to investigate the propagation of a high intensity ($I \sim 10^{21}$ Wcm^{-2}) laser in foam targets with densities ranging from $0.9n_c$ to $30n_c$. Proton acceleration was used to diagnose the interaction. An improvement in proton beam energy and efficiency is observed for the lowest density foam ($n_e = 0.9n_c$), compared to higher density foams. Simulations show that the laser beam penetrates deeper into the target due to its relativistic propagation, and results in greater collimation of the ensuing hot electrons. This results in the rear surface accelerating electric field being larger, increasing the efficiency of the acceleration. Enhanced collimation of the ions is seen to be due to the self-generated azimuthal magnetic and electric fields at the rear of the target.

PACS numbers: 52.38.Hb, 52.27.Ny, 52.38.Kd, 52.65.Rr

At the limit of currently achievable laser intensities ($I \sim 10^{21}$ Wcm^{-2}), the motion of electrons in a laser field can become highly relativistic, i.e. their normalised momentum $a_0 = eE_L/m_e\omega_0 c \gg 1$. The increased relativistic inertia of the electrons leads to a correction to the plasma frequency, ω_{pe}. A consequence of this is that the critical density, n_c, is increased to $n_{\gamma c} = \langle\gamma\rangle\, n_c$, where the time averaged $\langle\gamma\rangle = \sqrt{1 + \langle a^2\rangle}$. This can lead to induced relativistic optical transparency [1], so that light can propagate through what would otherwise be overdense plasma [2]. Aside from being of fundamental interest, this high-intensity critical-density regime is particularly important for the fast ignition concept of inertial confinement fusion [3], where the energy of a high intensity laser is converted into hot electrons to act as a localised spark for ignition. Additionally a preceding high-intensity beam, which may be used to bore a path to the high density core for the ignitor beam, would also interact with near-critical plasmas [4].

Critical density plasma interactions are difficult to diagnose because it is challenging to optically probe the interaction region directly. However, the interaction can be characterized by measurements of secondary emission, such as energetic electrons, ions or x-rays. For near-critical targets, the high-intensity laser energy can be transferred to plasma electrons through a number of mechanisms; both underdense ones such direct laser acceleration [5], as well as overdense mechanisms such as vacuum [6] and $j \times B$ heating [7]. As the hot electrons attempt to leave the target and move into the surrounding vacuum, a large space-charge electric field is generated. Ions can be accelerated to 10s of MeV in a direction normal to the rear target surface by this sheath field. This is known as target normal sheath acceleration (TNSA). Hence, the ion acceleration is highly dependent upon the efficiency of the electron acceleration by the laser [8].

Ion acceleration has been little studied from near-critical density plasmas. Shock acceleration is expected to be interesting in this regime, because the shock velocity, $v_{sh} \propto 1/\sqrt{n_e}$ [9]. In underdense plasmas both the TNSA [10] and shock acceleration [11] mechanisms have been observed experimentally using ultra-intense laser pulses. Time-varying magnetic field effects can also induce an electric field to accelerate ions and aid collimation [12]. Numerical work [13] suggests that TNSA may reach an optimum just below the critical density, depending on laser parameters and target thickness.

In this Letter, we present experimental evidence for relativistically induced optical transparency in near critical density plasma, $n_e \gtrsim n_c$. Measurements of proton acceleration from the rear surface of foam targets showed a marked increase in in number and energy as target n_e is reduced towards n_c, implying a change in the laser propagation. Two-dimensional particle-in-cell simulations show that this is because the laser propagates significantly further than predicted by the hole boring model [14] due to the relativistic dependence of the critical density.

The experiment was performed using the Vulcan Petawatt laser, which delivered an energy of $\mathcal{E}_L = 270 \pm 70$ J on target in a full-width-half-maximum (FWHM) pulse length of $\tau_L = 560 \pm 150$ fs. It was focused with an $f/3$ off-axis parabola to a $w_0 = 5.0 \pm 0.5$ μm FWHM focal spot diameter to produce a mean cycle-averaged peak intensity of $(8.0 \pm 3.4) \times 10^{20}$ Wcm^{-2} in vacuum, which corresponds to $a_0 \approx 36$. The laser is linearly polarised and operates at wavelength $\lambda = 1.054$ μm. Therefore, the non-relativistic critical density is $n_c = 1.0 \times 10^{21}$ cm^{-3}.

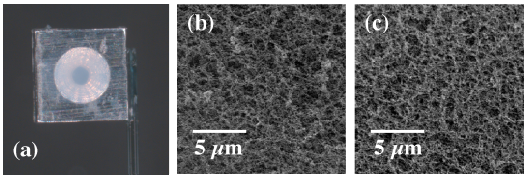

FIG. 1: (color online) (a) A washer holding the foam, and (b), (c) are high magnification photos showing the structure sizes for the 3 and 20 mg/cm^3 foams.

For a peak $a_0 \lesssim 36$, $n_{\gamma c} \lesssim 25\, n_c$.

The 250 μm thick low density foam targets were fabricated using the in-situ polymerisation technique and had a composition of 71% C, 27% O and 2% H by mass. Due to the delicate nature of the foams, they were mounted in 250 μm thick washers as shown in Fig. 1(a). The mass densities of the foams used were $\rho = 3$, 10, 15, 20, 45 and 100 mg/cm^3, which, assuming a fully ionised plasma is produced, gives electron number densities of $n_e = 0.9n_c$, $3n_c$, $4.5n_c$, $6n_c$, $13.5n_c$, $30n_c$ respectively. However, the laser intensity needs to reach $\sim 4 \times 10^{19}$ Wcm^{-2} before the foam will become fully field ionized. Therefore it may be expected that for a gaussian pulse with FWHM $\tau_L \sim 550$ fs, around 1.5% of the laser energy would arrive before this threshold is reached, i.e. the leading edge encounters an underdense plasma. Indeed by monitoring the transmitted laser energy after the interaction with burn paper, it was estimated that a few joules of laser energy (equivalent to a couple of percent) was transmitted through the 3, 20 and 45 mg/cm^3 foams (N.B. no data is available for the 100 mg/cm^3). The signal level was fairly constant over this density range, which is consistent with the leading edge of the pulse being transmitted.

Fig. 1 shows high magnification images of the foams. The pore and thread structures are small. The 5 μm scale indicated is w_0. The $\sim$ ns pre-pulse, of contrast ratio $\sim 10^{-7}$, was of sufficient intensity to partially ionize the foam. A conservative estimate of the pre-pulse heating suggests that at least the focal spot region would be homogenised before the arrival of the main pulse. However, it is likely that some structure may remain further into the target. It should be noted that this structure is significantly smaller than in foams used previously for high intensity laser interactions with foam targets which reported bulk [15] and Coloumb explosion ion acceleration [16]. The foam targets were shot at 0° incidence. Comparison shots onto 10 μm mylar targets, which have a similar line density, were shot at 45° to minimise the effect of back reflections and debris. On-axis electron spectra were measured on some shots using a magnetic spectrometer. The protons were recorded using 2 different types of stack. A simple stack made from CR39 nuclear track detector interleaved with iron produced a low energy resolution measurement of the maximum proton energy. The CR39 detector is capable of recording a much lower proton flux than the Cu activation stack. A copper activation stack was fielded for other shots, which uses proton-copper nuclear activation reactions to measure the total yield and proton spectrum for the entire beam [17]. Multiple layers of copper interleaved with radiochromic film (RCF) which record the proton beam divergence. Copper occurs naturally as two isotopes, 69.2% of ^{63}Cu and 30.8% of ^{65}Cu. ^{63}Cu(p, n)^{63}Zn and ^{65}Cu(p, 3n)^{63}Zn reactions both produce ^{63}Zn, which decays by β^+ emission with a characteristic half-life, $t_{1/2} = 38.47$ minutes. A γ flux generated by the energetic electron beam traveling through the stack was expected. However there are no γ reactions with the copper isotopes which generate ^{63}Zn. Hence the activation due to ^{63}Zn is a measure of the proton spectrum alone. The activity of each layer at three different times after the shot was measured using an absolutely calibrated coincidence counter, consisting of two head-on scintillator/photomultiplier tubes, which measure coincidence of the two oppositely directed 511 keV photons produced from β^+ annihilation. The other possible β^+ emitting isotopes have different $t_{1/2}$ and this enables the initial number of ^{63}Zn to be calculated for each layer from the measured activities. The sensitivity of each of the copper layers in terms of the number of activated atoms produced per incident proton as a function of proton energy was found using nuclear reaction cross-section data [18] and accounting for the changing proton spectra as energy is lost when passing through the different stack materials [19]. From this the proton spectra can be found using an iterative random perturbation method [17].

For the $\rho = 3$, 10 and 15 mg/cm^3 targets, high energy (> 20 MeV) on-axis *electron* spectra were observed with energies up to 85 ± 5 MeV and effective temperatures, T_e, up to 13.5 ± 0.2 MeV. However, for the 10 μm mylar target, no electrons were measured above the spectrometer low energy threshold (20 MeV). This indicates that the electron acceleration from the near critical density plasma, is more effective at producing high energy and temperature electron beams than from solid interactions.

Experimental proton spectra are shown in Fig. 2(a). The $\rho = 20$, 45 and 100 mg/cm^3 do not produce such high energy protons as the 10 μm mylar. Indeed if anything there is a gradual decrease in maximum energy, $\mathcal{E}_{p,max}$, (as defined as the energy at which there are 10^8 protons / MeV, filled squares) with decreasing ρ (Fig. 2(b)). However there is a marked increase in proton acceleration for the lowest density $\rho = 3$ mg/cm^3 target, with the spectrum extending to ~ 35 MeV as was the case for the mylar target. The open squares in Fig. 2(b) show the maximum measured proton energies from the CR39 stacks for more low plasma densities and show similarly high $\mathcal{E}_{p,max}$ (defined as the final CR39 record of the proton beam). For the mylar tar-

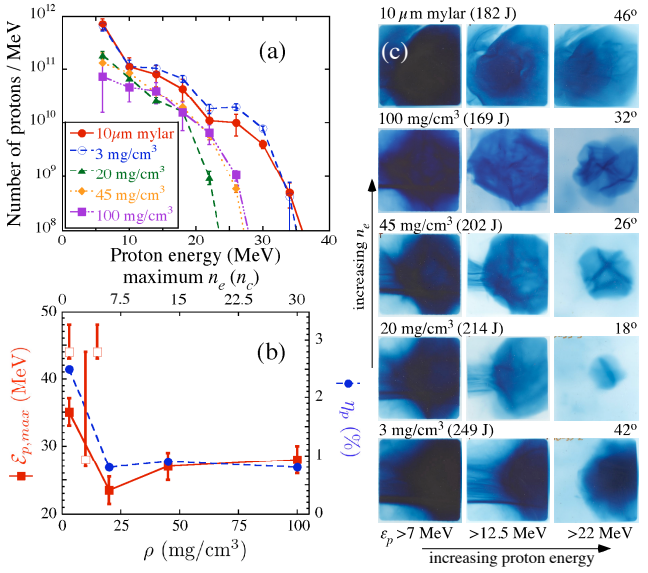

FIG. 2: (a) Proton spectra of the whole beams obtained from the Cu activation stacks. (b) Experimental trends for $\mathcal{E}_{p,max}$ and η_p (open squares are CR39 stack $\mathcal{E}_{p,max}$). (c) Proton beam profiles recorded by RCF interleaved in the Cu activation stacks. The labels at the top show ρ and $\mathcal{E}_L$. The angles indicate the FWHM of the proton beams for the > 22 MeV protons.

get, $\mathcal{E}_{p,max} = 28 \pm^{+16}_{-0.5}$ MeV. The conversion efficiency of on-target laser energy into protons with energies of > 4 MeV, η_p, is also shown on Fig. 2(b) and shows the same behaviour as $\mathcal{E}_{p,max}$. For the mylar target, $\eta_p = 3.1\%$.

Fig. 2(c) shows RCF pieces at different depths into the activation stack. Due to the peaked maximum of proton energy deposition at close to the maximum range (the Bragg peak) each film is characteristic of a different energy within the proton beam, and can be used to record the proton beam profile at that energy. The labels at the top of each line indicate the target and laser energy on target, the labels at the bottom show the minimum proton energy required to reach the layer (and hence the energy which contributes most to the signal) and the angle indicates the divergence of the proton beams for the ~ 22 MeV protons. The 3 mg/cm^3 foam for this shot was aligned at $\approx 10°$ to the laser axis and a similar angular shift is seen in the proton beam profile. This provides evidence that the proton beam was accelerated normal to the target surface by the TNSA mechanism. For all of the targets there is a reduction in the angular divergence of the proton beam with increasing proton energy. The foams produced more collimated beams than the 10 μm mylar target. This suggests that additional fields may be present that cause collimation of the ion beam. Structures visible particularly for high ρ shots, suggest that the target rear surface may have been less homogenized as target structures have been imprinted onto the proton beam profile at high energy [20]. Modulated proton beam profiles have also been attributed to non-homogeneous electron-beam transport through the target [21].

Simulations were performed to investigate the interactions at near critical density using the 2D3V particle-in-cell code OSIRIS [22]. A stationary box was used to investigate the ion acceleration. The simulation box was 251×251 μm with a resolution of 41.9 cells/λ in the longitudinal (x) direction and 25.13 cells/λ in the transverse direction (y). The ion acceleration was investigated for various initial n_e of $0.9n_c$, $1.5n_c$, $3n_c$, $4.5n_c$, $15n_c$, and $30n_c$. The density profile had a 1 μm long linear density ramp at the front of the plasma, 158 μm of plasma at maximum density, a 1 μm density ramp at the back of the target into a further 84 μm of vacuum. The laser pulse was linearly polarised with the electric field in the y-direction, with a FWHM $\tau_L = 500$ fs and $\lambda = 1.053$ μm. It was focused to $w_0 = 8$ μm at the top of the front density ramp, to give a peak vacuum $a_0 \approx 15$. The lowered value for the simulation intensity is to account for the fact that electron acceleration via DLA can overestimate the beam energy in 2D simulations due to betatron resonance being reached more quickly than in 3D.

Fig. 3 shows the ion density at a time of 2.0 ps into the simulation for each run. By this time, the laser has left the simulation box (or been absorbed) and the ion density is a good indication of the extent of the laser propagation d_{sim} for each case. The laser propagates through the entire plasma thickness for the $0.9n_c$ and $1.5n_c$ plasma. Strong filamentation and self-focusing of the laser energy is observed. For the $0.9n_c$ simulation, the average direction of the laser energy changes by as much as 17° and self-focuses to a peak $a_0 \approx 37$, more than double the vacuum value. Such large propagation instabilities could have serious implications for the hole boring fast ignition scheme. Individual laser filaments lead to the electron acceleration also becoming filamented.

d_{sim} decreases rapidly with increasing initial n_e, as can be seen in Fig. 4(a). Note that for $0.9n_c$ and $1.5n_c$ the laser emerges into the rear vacuum so could have propagated further. Using the ponderomotive hole boring velocity [14], $v_{hb} = \sqrt{I/m_i n_i c} = a_0 c\sqrt{(m_e n_c/2m_i n_e)}$ and $a_0 = 15$ for $\tau_L = 500$ fs gives an estimate for $d_{hb} = v_{hb}\tau_L \propto 1/\sqrt{n_e}$. This is equivalent to the time taken for the back of the pulse to catch up with the forward going shock and be either absorbed or reflected. The comparison of d_{hb} with d_{sim} agree well at high n_e, as shown in Fig. 4(a). However, there are large discrepancies at low n_e.

For $n_e < n_{\gamma c}$ the plasma is relativistically transparent and the propagation length is determined by the distance over which the laser beam is absorbed. An estimate of this length can be made by assuming that the laser energy, $\mathcal{E}_L = c\tau_L A\epsilon_0 (m_e c\omega_L/e)^2 \langle a^2 \rangle$, where A is the focal area of the laser, is entirely converted into hot electrons.

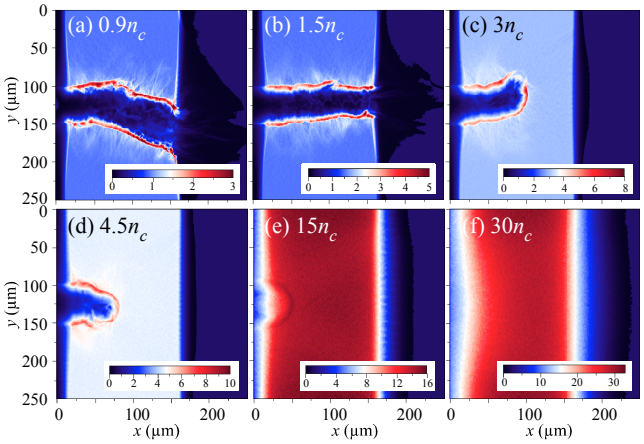

FIG. 3: The ion densities at 2.0 ps into the simulation.

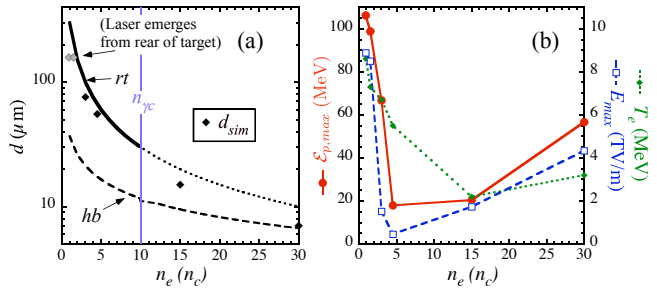

FIG. 4: (color online) (a) Variation of d_{sim} with n_e, predictions from the hole boring (hb) and relativistically induced transparency (rt) models and (b) E_{max} (at 1.2 ps), $\mathcal{E}_{p,max}$ (at 1.4 ps) and T_e (at 1.0 ps) seen in the simulations.

Although the absorption process is complex, a constant absorption rate can be assumed, with the average kinetic energy gained by an electron being the ponderomotive energy, $(\langle\gamma\rangle - 1)m_e c^2 = \frac{1}{2}\langle a^2\rangle m_e c^2$ for $n_e < n_{\gamma c}$. The total energy required to produce a channel of length d will therefore be $\mathcal{E}_{pe} = \frac{1}{2}\langle a^2\rangle m_e c^2 n_e A\, d$. Equating these energies gives $d_{rt} = 2c\tau_L n_c/n_e = 300\,(n_c/n_e)\,\mu$m and is shown in Fig. 4(a) as a solid line, (as a dashed line above $n_e = 10\,n_c = n_{\gamma c}$ for $a_0 = 15$) and agrees well with d_{sim}.

As n_e is increased the laser is able to penetrate less far, making a shorter cavity in the plasma. The area the electron beam emerges from at the rear of the target increases as their propagation distance through the target is longer. Hence the rear surface electric field E_{max} reduces and becomes more uniform, resulting in less ion acceleration [23]. This effect is partially compensated by the increased number of hot electrons at higher n_e. When the laser propagates further, as at $0.9n_c$ and $1.5n_c$, static electric and magnetic fields in the channel act to collimate the electrons and therefore when the laser emerges from the rear side of the target, the electrons emerge from a smaller region and therefore generate a larger E_{max}. Indeed, the simulation trends of $\mathcal{E}_{p,max}$, E_{max} and T_e seen in Fig. 4(b) show the same general dependence as observed experimentally, falling off at around n_c before recovering with increased density. Higher electron current could also aid the ion beam collimation [12, 13].

Shock acceleration is also seen originating from the front surface, particularly in the $n_e = 3n_c$–$15n_c$ simulations. However due to the efficiency of hot electron generation, the energy of the shock accelerated ions is always less than those accelerated at the rear surface.

Structure is also seen in the accelerated protons in the simulations, particularly at the lowest n_e, despite the plasma being initially uniform. The laser pulse evolves the ion structure on the rear plasma vacuum interface so that the density is increased in the walls of the cavity.

In conclusion, proton acceleration has been used to diagnose the propagation of a highly relativistic laser pulse through near critical density plasma. A dramatic increase in proton acceleration for decreasing plasma density approaching n_c was observed. Simulations show that the proton acceleration is enhanced by the laser propagation, which is not only due to hole-boring but must in part be explained by propagation in the relativistic transparent regime. Relativistic optically induced transparency would be beneficial for a fast ignition beam, allowing absorption at a higher density and closer to the fusion core, however the observed propagation instabilities may be problematic for the realisation of this scheme.

The authors acknowledge the staff of the Central Laser Facility (RAL) for technical assistance. We gratefully acknowledge the OSIRIS consortium (UCLA/IST/USC) for the use of OSIRIS and J. R. Davies for useful discussions. This work was supported by EPSRC under grant No. GR/T25934/01.

† Present address: Institut für Optik und Quantenelektronik, Friedrich-Schiller-Universität Jena, Germany
* Present address: Center for Ultrafast Optical Science, University of Michigan, Ann Arbor, MI 48109, USA
‡ Present address: University of Rochester - Laboratory for Laser Energetics, Rochester, NY 14623, USA

[1] P. Kaw and J. Dawson, Phys. Fluids, **13**, 472 (1970); P. Sprangle *et al.*, IEEE Trans. Plas. Sci. **PS-15**, 145 (1987); S. Guérin *et al.*, Phys. Plas., **3**, 2693 (1996); J. C. Adam *et al.*, Phys. Rev. Lett., **78**, 4765 (1997).
[2] J. Fuchs *et al.*, Phys. Rev. Lett., 80, 2326 (1998).
[3] M. Tabak *et al.*, Phys. Plas. **1**, 1626 (1994).
[4] G. Li *et al.*, Phys. Rev. Lett., **100**, 125002 (2008).
[5] A. Pukhov and J. Meyer-ter Vehn, Phys. Plas., **5**, 1880 (1998).
[6] F. Brunel, Phys. Rev. Lett. **59**, 52 (1987).
[7] W. L. Kruer and K. Estabrook, Phys. Flu. **28**, 430 (1985).

[8] J. Schreiber *et al.*, Phys. Rev. Lett. **97**, 045005 (2006).
[9] L. O. Silva *et al.*, Phys. Rev. Lett. **92**, 15002 (2004).
[10] L. Willingale *et al.*, Phys. Rev. Lett. **96**, 245002 (2006).
[11] M. S. Wei *et al.*, Phys. Rev. Lett. **93**, 155003 (2004).
[12] T. Zh. Esirkepov, *et al.*, JETP Lett., **70**, 82 (1999)
[13] L. Willingale *et al.*, accepted by IEEE Trans. Plas. Sci. (2008).
[14] S. C. Wilks *et al.*, Phys. Rev. Lett. **69**, 1383 (1992).
[15] Y. T. Li *et al.*, Phys. Rev. E **72**, 66404 (2005).
[16] S. Okihara *et al.*, Phys. Rev. E **69**, 26401 (2004).
[17] E. L. Clark, Ph.D. thesis, University of London (2001).
[18] EXFOR database online at http://www.nndc.bnl.gov
[19] M. J. Berger *et al.*, PSTAR, available at https://physics.nist.gov/Star (2007).
[20] T. E. Cowan *et al.*, Phys. Rev. Lett. **92**, 204801 (2004).
[21] J. Fuchs *et al.*, Phys. Rev. Lett., **91**, 255002 (2003).
[22] R. O. Fonseca *et al.*, Lecture Notes in Computer Science **2331**, 342 (2002).
[23] T. Esirkepov *et al.*, Phys. Rev. Lett. **96**, 105001 (2006).